metals

MDPI

Article

Effect of Load Partitioning Under Different Pressing Temperature Conditions During 2P1A Compaction on the Densification Behavior and Electromagnetic Properties of Fe–5.0 wt.%Si SMC Core

Minseop Sim [1] and Seonbong Lee [2,*]

[1] Department of Mechanical Engineering, Keimyung University, Daegu 42601, Republic of Korea; 5587911@stu.kmu.ac.kr
[2] Department of Automotive Engineering, Keimyung University, Daegu 42601, Republic of Korea
* Correspondence: seonbong@kmu.ac.kr; Tel.: +82-10-5180-5067

Abstract

Soft magnetic composites (SMCs) are attracting increasing attention for electromagnetic applications owing to their three-dimensional shape flexibility and reduced eddy current loss. In this study, the 2-Pressing 1-Annealing (2P1A) process was applied to Fe–5.0 wt.%Si SMC toroidal cores to investigate the effects of pressing temperature and 1st pressing level on densification behavior, interparticle insulation structure, and frequency-dependent electromagnetic response. DEFORM-3D FEM simulations compared relative density distribution, hydrostatic stress, effective strain, and reaction load under single-press and 2P1A conditions. The 1st pressing stage was conducted at 350 °C with 30%, 50%, and 70% pressing levels, followed by final densification at 550 °C. Increasing compaction temperature reduced reaction load and hydrostatic stress range, while the 1st pressing level affected the final density distribution and stress state after 2nd pressing. TEM-EDS confirmed continuous interparticle insulation layers, and thickness measurements were used to compare local boundary structures. Among the 2P1A conditions, the 50% → 100% condition showed the smallest upper/lower relative density difference and the narrowest insulation-layer thickness range, indicating the most balanced condition in terms of densification uniformity and interparticle boundary structure. Compared with the 550 °C single-press condition, the 2P1A compacts showed higher permeability retention and Q-factor values in the 5–20 kHz range. These results indicate that the 1st pressing level influences staged densification behavior, interparticle boundary structure, and frequency-dependent electromagnetic response in Fe–5.0 wt.%Si SMC cores.

Keywords: soft magnetic composite (SMC); 2P1A compaction; load-partitioned compaction; staged densification; interparticle insulation structure; electromagnetic properties; AFPM stator core

Check for updates

Received: 19 May 2026
Revised: 10 June 2026
Accepted: 12 June 2026
Published: 17 June 2026

Copyright: © 2026 by the authors. Licensee MDPI, Basel, Switzerland. This article is an open access article distributed under the terms and conditions of the Creative Commons Attribution (CC BY) license.

1. Introduction

SMCs are powder-based soft magnetic materials fabricated by high-temperature compaction of ferromagnetic powders coated with electrically insulating layers [1–4]. Recently, the automobile industry and electric mobility sector have increasingly demanded high-power and high-efficiency vehicle traction motors, leading to growing interest in low-loss soft magnetic core materials and compaction processes capable of producing complex-shaped components [2,3,5–8]. SMCs can reduce eddy current loss through particle-scale

insulation structures and offer advantages in fabricating complex three-dimensional core geometries through powder compaction processes [1–4,7,9–12]. Owing to these characteristics, SMCs have been continuously investigated for applications requiring geometric flexibility and three-dimensional magnetic flux paths, such as toroidal cores, inductor cores, and axial flux permanent magnet (AFPM) structures [3,5–7,10–12].

The electromagnetic properties of SMC cores are influenced not only by alloy composition and insulation-layer formation conditions but also by the density, densification state, and interparticle contact structure formed during the compaction process [2–4,8,11,13–17]. During powder compaction, particle rearrangement, plastic deformation, die-wall friction, and local densification occur simultaneously, determining the density distribution, stress state, and microstructural uniformity of the final compact [13–16,18–21]. Increased compaction density is generally advantageous for maintaining continuous magnetic flux paths and mechanical stability; however, excessive compaction load or non-uniform densification may induce insulation-layer damage, residual stress concentration, and increased electromagnetic loss [8,11,14–20,22]. Therefore, securing stable electromagnetic performance in SMC cores requires consideration of densification behavior and stress state during compaction rather than simply increasing the final compaction pressure [2–4,8,13–20,22].

Previous SMC studies have mainly focused on the effects of alloy composition, insulation coating layers, heat treatment conditions, and compaction pressure on density and electromagnetic properties. FEM-, DEM-, and MPFEM-based analyses have also been employed to investigate densification behavior and stress distribution during powder compaction [13–15,18–21,23–25]. However, most studies have concentrated on material conditions, single-press compaction, or final property evaluation, while relatively few studies have investigated how different first pressing levels in a two-stage pressing process affect densification behavior during subsequent high-temperature pressing and the resulting electromagnetic properties [8,19,25–30]. In particular, studies on Fe–Si-based SMCs that combine 2P1A processing with different first pressing levels together with FEM analysis and experimental evaluation of microstructure and electromagnetic properties remain limited [2–4,6–8,17,22,26–30].

The 2P1A process applied in this study was designed not merely to increase the number of pressing cycles, but to control staged densification behavior by separating the 1st pressing stage from the 2nd high-temperature pressing stage [8,19,26–30]. Conventional single-press compaction generally requires high compaction loads to secure the target density, often accompanied by local densification and stress concentration [13–16,18–21]. In contrast, when different first pressing levels are introduced during the 1st pressing stage and final compaction is subsequently performed under high-temperature conditions during the second pressing stage, staged densification behavior and local density distribution can be controlled according to the first pressing level [7,18]. However, excessively low first pressing levels may induce abrupt deformation during the second pressing stage, whereas excessively high first pressing levels may already generate local densification and stress concentration during the first stage [13–16,18–21]. Therefore, the first pressing level can be regarded as a key process parameter influencing staged densification behavior and electromagnetic properties in the 2P1A process [8,19,26–30].

To investigate first pressing level-dependent staged densification behavior, Fe–5.0 wt.%Si-based SMC toroidal cores were employed in this study. Toroidal cores are representative specimens widely used to evaluate permeability, Q-factor, and frequency-dependent magnetic response in SMC materials [3,10–12,27–31]. In addition, the ring geometry is suitable for comparing local densification differences between upper and lower regions generated during compaction [13–16,18–21]. Therefore, the toroidal geometry was selected

as a reference specimen for analyzing local density distribution, interfacial structure, and electromagnetic response according to the first pressing condition [3,8,10–12,26–31].

In this study, DEFORM-3D plastic deformation analysis was conducted to evaluate the densification behavior of Fe–5.0 wt.%Si SMC toroidal cores under single-press and 2P1A compaction routes. Based on the FEM results, representative processing conditions were selected for bulk fabrication and subsequent characterization. SEM and TEM-EDS analyses were conducted to examine the densification morphology and interparticle insulation structure, while permeability and Q-factor measurements were performed to evaluate the frequency-dependent electromagnetic response [5,6,9,11,12,21,22,31–33]. Through these analyses, this study aimed to clarify how the 1st pressing level in load-partitioned 2P1A compaction influences densification behavior, interparticle insulation-layer structure, and electromagnetic response in Fe–5.0 wt.%Si SMC toroidal cores [2–4,6–8,10–12,26–30].

2. Materials and Methods

2.1. Fe–5.0 wt.%Si SMC Powder

Fe–5.0 wt.%Si alloy powder fabricated by the water atomization process was used to fabricate toroidal SMC compacts [8,26]. The nominal powder composition followed that reported in a previous study [25]. The powder composition was measured by XRF analysis, and the average particle size was defined using the Dv50 value [30,31]. Table 1 summarizes the material parameters used for compaction experiments and FEM analysis. The Fe, Si, and O contents were measured as 94.85, 5.02, and 0.13 wt.%, respectively, while the Dv50 value was 79.136 μm.

Table 1. Material parameters of the Fe–5.0 wt.%Si powder used for compaction experiments and FEM analysis.

Parameter	Value
Fe content (wt.%)	94.85
Si content (wt.%)	5.02
O content (wt.%)	0.13
Dv50 (μm)	79.136
Tap density (g/cm^3)	3.34
True density (g/cm^3)	7.80
Initial relative density	0.428

For FEM analysis, the true density of the Fe–5.0 wt.%Si powder was set to 7.80 g/cm^3 [26–30]. This value was used as the reference density for converting tap density and compact density into relative density. The tap density of the powder was 3.34 g/cm^3, and the initial relative density before compaction was calculated as 0.428.

The additive composition consisted of 0.25 wt.% H_3PO_4 (HP), 0.25 wt.% polyimide (PI), 1.0 wt.% MoS_2, and 0.3 wt.% graphite. The additives were blended with the Fe–5.0 wt.%Si powder prior to compaction. H_3PO_4 and polyimide were introduced for insulation-layer formation and binder functions, while MoS_2 and graphite were used as lubricant additives to reduce powder–die and interparticle friction during pressing [22,32–34].

2.2. Design of Single-Press and 2P1A Compaction Conditions

Figure 1 shows the overall compaction process applied in this study. In conventional single-press compaction of SMC materials, the entire compaction load is applied during a single pressing stage. In ring-type geometries such as toroidal cores, differences in constraint conditions between the inner and outer regions may induce local densification differences during compaction [14,19].

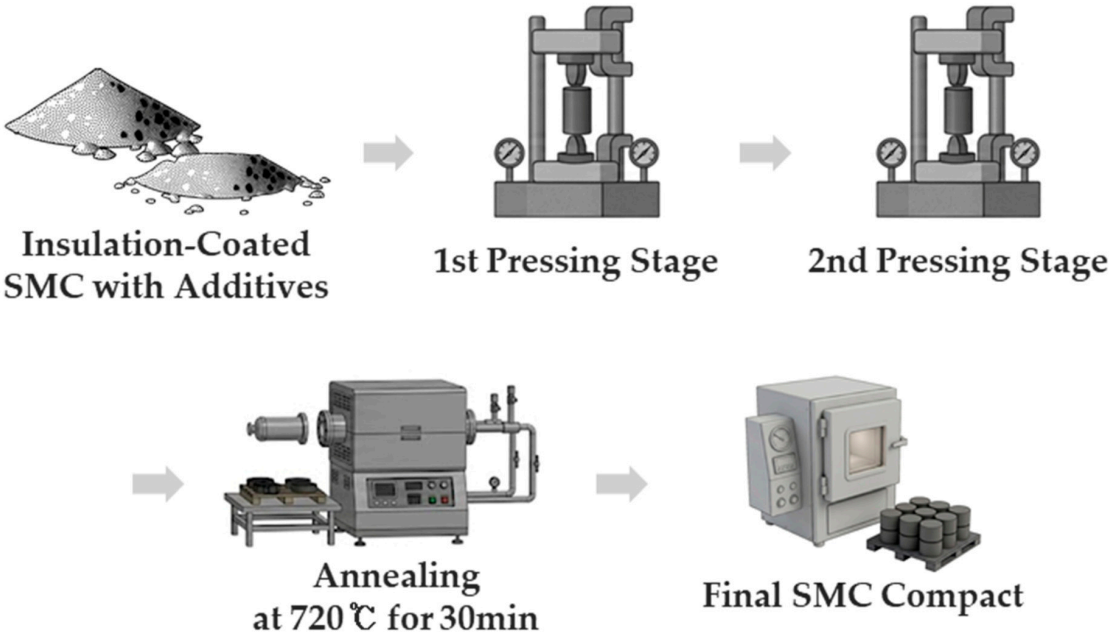


Figure 1. Schematic illustration of the 2P1A process flow for SMC compacts.

In this study, 2P1A process with different first pressing levels was designed based on conventional single-press compaction. The 2P1A process consists of 1st pressing, 2nd pressing, and final annealing, and the present study focused on the effect of the first pressing level within this process [8,26,27].

"Before establishing the 2P1A conditions, single-press FEM simulations were first conducted under RT, 350 °C, and 550 °C conditions. The RT condition was used as the room-temperature compaction reference, while the 350 °C and 550 °C conditions were selected to compare compaction behavior under warm and hot compaction conditions." Under identical toroidal geometry and powder charging conditions, only the pressing temperature was varied to compare relative density distribution, reaction load, hydrostatic stress, and effective strain behavior [15,16,35–37].

For the 2P1A simulations, the first pressing temperature was set to 350 °C, and the 1st pressing levels were classified as 30%, 50%, and 70% of the reference reaction load. The three 1st pressing conditions were applied to compare how the first pressing level affected the subsequent densification behavior at 550 °C.

To determine the pressing temperatures, the temperature-dependent thermal conductivity and friction behavior of the Fe–5.0 wt.%Si SMC system were evaluated. The thermal conductivity was measured using the laser flash method (LFA427, NETZSCH, Selb, Germany), and the results are summarized in Table 2. The increase in thermal conductivity was relatively large from room temperature to 300 °C, whereas the increase became relatively small in the 300–600 °C range. Above 600 °C, the thermal conductivity tended to decrease. Based on this tendency, 350 °C and 550 °C were preliminarily selected as the first and second pressing temperatures, respectively. The friction coefficient was then evaluated using high-temperature reciprocating friction tests conducted with a multi-purpose wear simulation system (UMT-Tribolab, Bruker, Bremen, Germany). The average friction coefficient decreased from 0.846 at room temperature and 0.751 at 150 °C to 0.509 at 350 °C and further decreased to 0.377 at 550 °C. Based on these characteristics, the first and second pressing temperatures were finally set to 350 °C and 550 °C, respectively [15,19].

Table 2. Thermal conductivity variation across temperature intervals for the Fe–5.0 wt.%Si SMC.

Temperature Interval (°C)	Thermal Conductivity Variation (W/mK)
0–100	1.3
100–200	2.4
200–300	0.5
300–400	0.3
400–500	1.4
500–600	0.2
600–700	1.6

2.3. Porous Material Model for Powder Compaction

Prior to the FEM analysis, the Fe–5.0 wt.%Si powder compact was modeled as a compressible porous material. The yielding and densification behavior of the powder compact are affected not only by equivalent stress, but also by hydrostatic stress and porosity [8,21]. The compaction behavior of the powder compact was expressed using the following porous plastic yield function:

$$\mathrm{F}(\sigma_{eq}, p, f) = \left(\frac{\sigma_{eq}}{\sigma_y}\right)^2 + \mathrm{A}(f)\left(\frac{p}{\sigma_y}\right)^2 - \mathrm{B}(f) = 0, \quad (1)$$

here σ_{eq}, p, f, σ_y represent the von Mises equivalent stress, hydrostatic pressure, porosity, and yield stress of the fully dense matrix material, respectively. A(f) and B(f) are functions describing changes in the yield surface according to porosity. The equation indicates that the compaction behavior of the powder compact is governed by deviatoric stress, hydrostatic stress, and porosity evolution during densification. Therefore, relative density, hydrostatic stress, effective strain, and reaction load were employed as the primary evaluation parameters in this study.

In the FEM analysis, porosity evolution was calculated using the porous material model in DEFORM-3D. The initial relative density was set to 0.428 using the tap density and true density listed in Table 1. During compaction, the local relative density was updated according to volumetric deformation and mass conservation.

2.4. FEM Modeling and Boundary Conditions

A finite element model was constructed using DEFORM-3D to analyze the densification behavior of Fe–5.0 wt.%Si toroidal compacts during single-press and 2P1A compaction. Considering the geometric symmetry of the toroidal core, a half-core model was employed. The workpiece was defined as a porous deformable body, while the upper punch, lower punch, and die were assumed to be rigid bodies [21].

The temperature-dependent flow stress data of the Fe–5.0 wt.%Si powder compact were constructed from compression test results measured at selected temperatures and fitted for use as the DEFORM-3D material input. The flow stress was defined as a function of strain, strain rate, and temperature, and the corresponding material response was applied to the RT, 350 °C, and 550 °C compaction simulations.

The initial powder compact geometry was determined based on the mass conservation relationship between the charged powder and the final compact. The powder charge was fixed at 10 g per specimen to reflect the experimental fabrication condition. The initial charging height for FEM modeling was calculated from mass conservation using the target bulk density of 7.3 g/cm^3 and the powder parameters listed in Table 1, including tap density, true density, and initial relative density. The toroidal geometry was defined with

an outer diameter of 20.38 mm and an inner diameter of 12.6 mm, corresponding to a ring cross-sectional area of approximately 2.015 cm^2.

Figure 2 shows the half-core FEM model and compaction sequence used in this study. Single-press simulations were performed at RT, 350 °C, and 550 °C, and all conditions were set to reach the same final geometry. The 2P1A conditions were subsequently constructed to compare staged densification behavior. Table 3 summarizes the single-press and 2P1A compaction conditions used in the FEM simulations. Cases 1–3 correspond to single-press conditions at RT, 350 °C, and 550 °C, respectively. Cases 4–6 correspond to 2P1A conditions in which 1st pressing levels of 30%, 50%, and 70% were applied at 350 °C, followed by final compaction at 550 °C. All cases were set to reach the same target compact height to compare differences in densification behavior according to the compaction path.

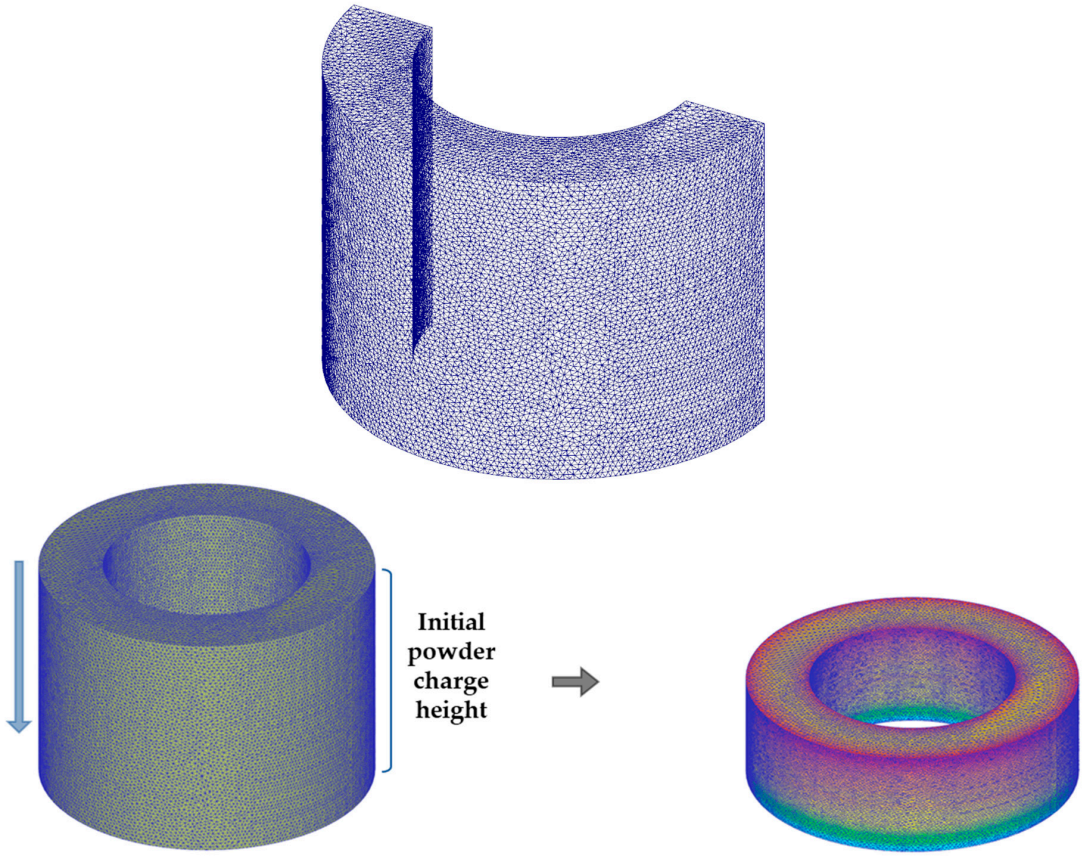


Figure 2. FEM half-core model and compaction sequence of the Fe–5.0 wt.%Si toroidal compact.

Table 3. FEM simulation conditions for single-press and 2P1A compaction.

Case	Compaction	1st Pressing Temperature	1st Pressing Condition	2nd Pressing Temperature	2nd Pressing Condition
Case 1	Single-press	RT	100%	–	Final height
Case 2	Single-press	350 °C	100%	–	Final height
Case 3	Single-press	550 °C	100%	–	Final height
Case 4	2P1A	350 °C	30%	550 °C	Final height
Case 5	2P1A	350 °C	50%	550 °C	Final height
Case 6	2P1A	350 °C	70%	550 °C	Final height

The 1st pressing levels in the 2P1A conditions were defined based on the reaction load obtained from the 350 °C single-press condition. The first pressing stage was performed at 350 °C until the target 1st pressing level was reached. The process temperature was

then changed to 550 °C, and the second pressing stage was subsequently performed. This compaction sequence was designed to analyze first pressing level-dependent staged densification behavior in the 2P1A process.

The contact condition between the workpiece and tooling was defined using temperature-dependent friction coefficients measured for the same Fe–5.0 wt.%Si powder and additive composition. As described earlier, the friction coefficient decreased from 0.846 at 25 °C to 0.751 at 150 °C, 0.509 at 350 °C, and 0.3769 at 550 °C. These temperature-dependent friction properties were used as input conditions to reflect the reduction in die-wall friction and lubrication effects during high-temperature compaction [33–36].

The die and lower punch were fixed as rigid bodies, and the powder compact was compressed by axial movement of the upper punch. A symmetry boundary condition was applied to the cut plane of the half-core model. Thermal conditions were assigned according to each compaction stage. The single-press simulations were performed under isothermal conditions at each temperature. In the 2P1A simulations, the temperatures of the workpiece and tooling were sequentially changed from 350 °C during the first pressing stage to 550 °C during the second pressing stage to reflect the staged thermo-mechanical compaction process. The workpiece mesh consisted of approximately 272,483 elements and 57,525 nodes.

3. FEM Analysis of Single-Press and 2P1A Compaction

3.1. Temperature Effect in Single-Press Compaction

Figures 3–5 and Table 4 show the FEM results for single-press compaction at RT, 350 °C, and 550 °C under the same final geometry condition. All three conditions were set to reach a final compact height of approximately 6.72 mm, and the effects of compaction temperature on relative density distribution, reaction load, hydrostatic stress, and effective strain distribution were compared. The average relative density was maintained at approximately 0.936 under all conditions, whereas the relative density difference decreased from 0.45 under the RT condition to 0.34 at 350 °C and 0.32 at 550 °C.

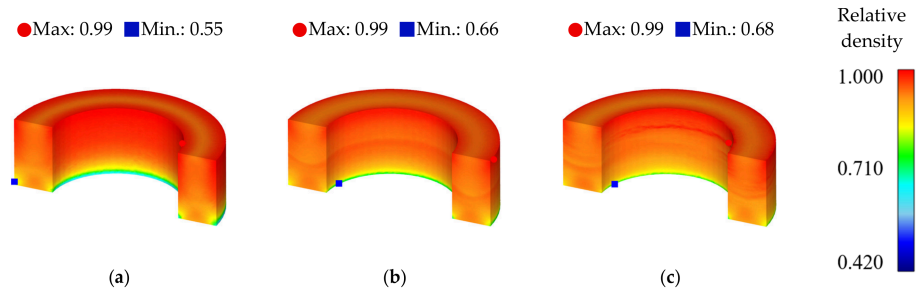


Figure 3. Relative density results: (**a**) Case 1, (**b**) Case 2, and (**c**) Case 3.

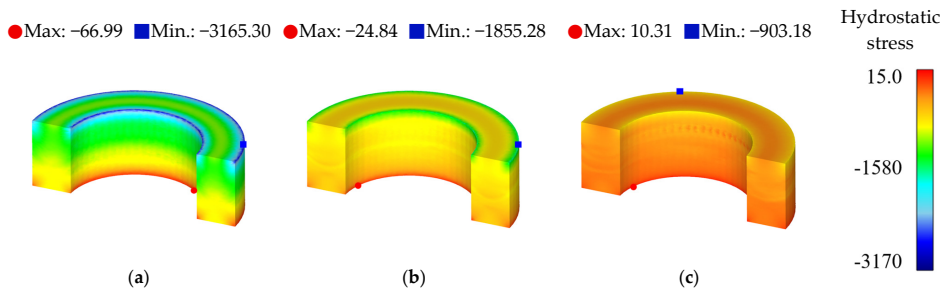


Figure 4. Hydrostatic stress results: (**a**) Case 1, (**b**) Case 2, and (**c**) Case 3.

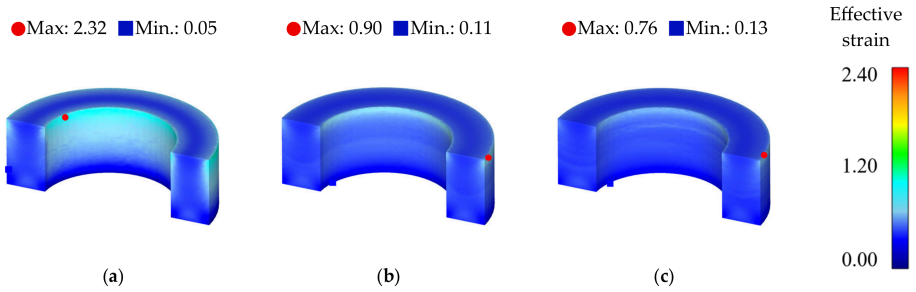


Figure 5. Effective strain results: (**a**) Case 1, (**b**) Case 2, and (**c**) Case 3.

Table 4. FEM results in Single-press compaction.

Case	Avg. Relative Density	Relative Density Difference (Max–Min)	Avg. Hydrostatic Stress (MPa)	Hydrostatic Stress Range (MPa)	Avg. Effective Strain	Effective Strain Range	Reaction Load (tons)
Case 1	0.936	0.45	−1220.35	3098.31	0.49	2.27	18.74
Case 2	0.936	0.34	−743.92	1830.44	0.46	0.80	10.78
Case 3	0.936	0.32	−400.49	913.50	0.45	0.63	5.58

The increase in compaction temperature directly reduced the reaction load. The reaction load was highest under the RT condition at 18.74 tons, decreased to 10.78 tons at 350 °C, and further decreased to 5.58 tons at 550 °C. These values correspond to reductions of approximately 42.5% and 70.2% compared with the RT condition, respectively. The decrease in the load required to reach the same final geometry indicates that powder rearrangement and compression proceeded with lower resistance under elevated-temperature conditions.

The hydrostatic stress distribution showed a stronger temperature dependence. The average hydrostatic stress was −1220.35 MPa under the RT condition, indicating the highest compressive stress state. The values decreased to −743.92 MPa at 350 °C and −400.49 MPa at 550 °C. The hydrostatic stress range was also highest under the RT condition at 3098.31 MPa, whereas it decreased to 1830.44 MPa at 350 °C and 913.50 MPa at 550 °C. The hydrostatic stress range decreased by approximately 40.9% at 350 °C and 70.5% at 550 °C compared with the RT condition. These results indicate that spatial variation in compressive stress was pronounced during RT compaction, whereas the stress distribution became more uniform under elevated-temperature conditions.

The effective strain distribution showed the same trend. The average effective strain was 0.49 under the RT condition and slightly decreased to 0.46 and 0.45 at 350 °C and 550 °C, respectively. However, the effective strain range showed a larger difference. The RT condition exhibited an effective strain range of 2.27, whereas the values decreased to 0.80 at 350 °C and 0.63 at 550 °C. Although the average values differed only slightly, the strain range differed markedly, indicating local strain concentration under the RT condition. In particular, the maximum effective strain reached 2.32 under the RT condition, while it was limited to 0.90 and 0.76 at 350 °C and 550 °C, respectively.

Overall, the RT single-press condition reached the same final geometry but required a high reaction load and exhibited large hydrostatic stress and effective strain ranges. In contrast, the 550 °C single-press condition showed the lowest reaction load and the most reduced stress and strain distributions, indicating the most stable mechanical compaction behavior among the single-press conditions. Accordingly, the 550 °C single-press condition was used as the reference condition for fabricated toroidal bulk compacts and electromagnetic property evaluation together with the 2P1A conditions.

However, the 2P1A process requires separation of the 1st pressing stage and the 2nd high-temperature pressing stage. Although the 550 °C single-press condition showed the most stable mechanical compaction behavior, this temperature corresponds to the 2nd pressing condition in the 2P1A process. Therefore, the 1st pressing stage required a temperature condition that reduced the excessive compaction resistance and stress/strain concentration observed under RT compaction while remaining distinct from the 550 °C condition used during the 2nd pressing stage. Based on this consideration, 350 °C was selected as the 1st pressing temperature for the 2P1A process, and 1st pressing levels of 30%, 50%, and 70% were defined based on the reaction load obtained from the 350 °C single-press condition.

3.2. 1st Pressing Effect in 2P1A Compaction

Based on the single-press results in Section 3.1, the 350 °C condition was selected as the 1st pressing temperature for the 2P1A process. The 1st pressing stage was performed under 1st pressing levels of 30%, 50%, and 70% based on the reaction load obtained from the 350 °C single-press condition. Table 5 summarizes the FEM results after the 1st pressing stage under each 1st pressing level. As the 1st pressing level increased, the average relative density increased from 0.561 to 0.827, while the compact height decreased from 11.21 mm to 7.61 mm. The reaction load also increased from 3.11 tons to 7.25 tons. These results indicate that the preliminary densification level during the 1st pressing stage was progressively controlled according to the 1st pressing level.

Table 5. FEM results after the 1st pressing stage in the 2P1A cases under different 1st pressing levels.

Case	1st Pressing Level	Avg. Relative Density	Compact Height (mm)	Reaction Load (tons)
Case 4	30%	0.561	11.21	3.11
Case 5	50%	0.722	8.71	5.18
Case 6	70%	0.827	7.61	7.25

Figures 6–8 and Table 6 show the final FEM results after the 2nd pressing stage, focusing on differences in internal stress and strain distributions according to the 1st pressing level. The relative density difference represents the difference between the maximum and minimum relative densities within the compact, where a smaller value indicates a more uniform relative density distribution. The relative density difference under the 2P1A conditions was 0.33, 0.34, and 0.43 for the 30%, 50%, and 70% 1st pressing levels, respectively. These values were lower than that of the RT single-press condition (0.45) and comparable to those of the 350 °C and 550 °C single-press conditions (0.34 and 0.32, respectively). Therefore, the 2P1A conditions reduced the large relative density variation observed under RT compaction while maintaining a relative density distribution comparable to those under elevated-temperature single-press conditions.

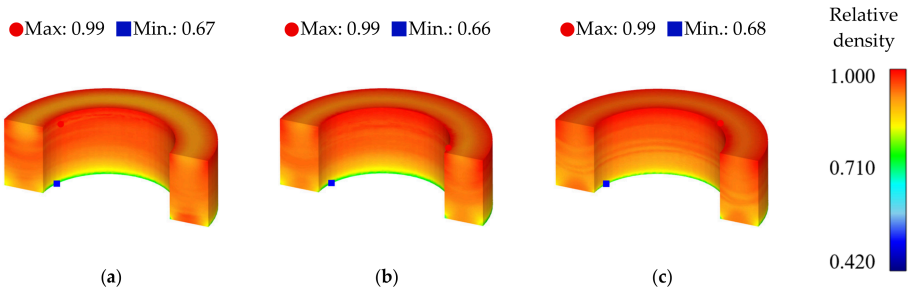


Figure 6. Relative density results: (**a**) Case 4, (**b**) Case 5, and (**c**) Case 6.

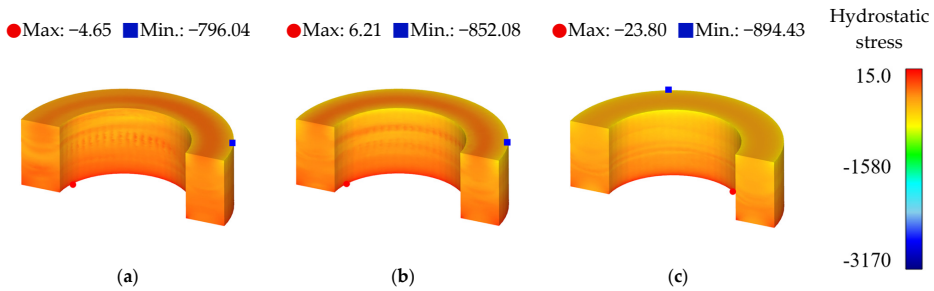


Figure 7. Hydrostatic stress results: (**a**) Case 4, (**b**) Case 5, and (**c**) Case 6.

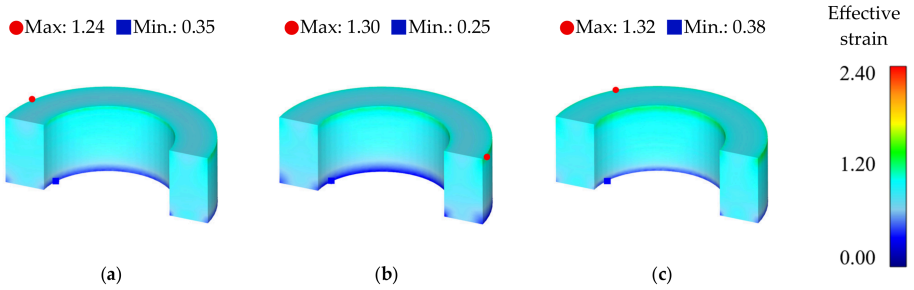


Figure 8. Effective strain results: (**a**) Case 4, (**b**) Case 5, and (**c**) Case 6.

Table 6. Final FEM results after second pressing in the 2P1A cases under different pressing conditions.

Case	1st Pressing Level	Avg. Relative Density	Relative Density Difference (Max–Min)	Avg. Hydrostatic Stress (MPa)	Hydrostatic Stress Range (MPa)	Avg. Effective Strain	Effective Strain Range	Reaction Load (tons)
Case 4	30%	0.936	0.33	−372.60	791.40	0.84	0.89	5.27
Case 5	50%	0.936	0.34	−403.98	858.28	0.80	1.05	5.73
Case 6	70%	0.936	0.43	−467.07	870.62	0.86	0.94	6.46

The hydrostatic stress distribution showed increasing average compressive stress and stress range with increasing 1st pressing level. The average hydrostatic stress values for Cases 4, 5, and 6 were −372.60, −403.98, and −467.07 MPa, respectively, while the hydrostatic stress ranges increased to 791.40, 858.28, and 870.62 MPa, respectively. These results indicate that higher compressive stress levels were already introduced during the 1st pressing stage at higher 1st pressing levels, resulting in increased stress accumulation during the 2nd pressing stage.

The average effective strain values for Cases 4, 5, and 6 were 0.84, 0.80, and 0.86, respectively, while the effective strain ranges were 0.89, 1.05, and 0.94, respectively. These values were higher than those of the 550 °C single-press condition, which exhibited an average effective strain of 0.45 and a strain range of 0.63. However, under the 2P1A conditions, densification did not occur during a single pressing stage. Instead, the 1st pressing stage and subsequent high-temperature densification were sequentially performed, resulting in increased accumulated plastic deformation. Therefore, the higher effective strain observed under the 2P1A conditions can be interpreted as a result of accumulated plastic deformation caused by separation of the 1st pressing stage and the 2nd high-temperature pressing stage.

The reaction load after the 2nd pressing stage increased from 5.27 tons to 5.73 tons and 6.46 tons for the 30%, 50%, and 70% 1st pressing levels, respectively. Although the 70% 1st pressing condition exhibited the highest preliminary densification level, it also showed the highest reaction load and compressive stress level during the final pressing stage.

These results indicate that increasing the 1st pressing level also increased the additional compaction resistance during final densification.

3.3. Comparison of Single-Press and 2P1A Compaction

Based on the FEM results presented in Sections 3.1 and 3.2, the single-press and 2P1A conditions exhibited different compaction behaviors. The 550 °C single-press condition showed the lowest reaction load and the smallest stress/strain ranges, indicating the most stable mechanical compaction behavior among the single-press conditions. In the 2P1A conditions, the final reaction load, hydrostatic stress, and relative density distribution varied depending on the 1st pressing level, and increasing the 1st pressing level did not lead to a consistent improvement in the final compaction state. In particular, the 70% → 100% condition showed the highest densification level after the 1st pressing stage, but it also exhibited the highest final reaction load and hydrostatic stress level.

These results indicate that the 1st pressing level in the 2P1A process affects not only the densification state after the 1st pressing stage but also the subsequent stress accumulation and final compaction state after the 2nd pressing stage. Based on these FEM results, four conditions—the 550 °C single-press condition and the 30% → 100%, 50% → 100%, and 70% → 100% 2P1A conditions—were selected for bulk fabrication, microstructural characterization, and electromagnetic property evaluation [10–12,16].

4. Experimental Validation of 2P1A Toroidal Compacts

4.1. Bulk Prototype Fabrication

Fe–5.0 wt.%Si toroidal compacts were fabricated to validate the compaction behavior and final bulk properties under the single-press and 2P1A conditions. To ensure consistency between the numerical and experimental investigations, the toroidal specimens were fabricated with the same dimensions as those employed in the FEM analysis (OD: 20.38 mm, ID: 12.6 mm). Each specimen was compacted using a powder charge of 10.0 ± 0.1 g. The toroidal compacts were fabricated using a 50-ton hydraulic press [19,20,34].

Figure 9 shows the fabricated Fe–5.0 wt.%Si toroidal compacts and wound specimens for electromagnetic measurements. Figure 9a corresponds to the 550 °C single-press condition, while Figure 9b–d correspond to the 30% → 100%, 50% → 100%, and 70% → 100% 2P1A conditions, respectively. Four toroidal compacts were fabricated for each condition, and the electromagnetic properties were compared using averaged values obtained from repeated measurements. The 550 °C single-press condition was selected as the comparison condition because it exhibited the lowest compaction resistance and the most stable stress/strain distribution in the FEM results presented in Section 3.

Under the 2P1A conditions, the 1st pressing stage was performed at 350 °C under 1st pressing levels of 30%, 50%, and 70% of the reference load, followed by 2nd pressing at 550 °C under the full pressing condition. Therefore, the 2P1A conditions were designed to compare changes in final compaction state and material properties according to the 1st pressing level by separating the 1st pressing stage and the 2nd high-temperature pressing stage.

To compare the FEM-predicted densification level with the fabricated compacts, the bulk densities of three specimens for each condition were measured and summarized in Supplementary Table S1. The bulk density of the fabricated specimens was measured as 7.31–7.34 g/cm^3, corresponding to relative densities of 0.937–0.941, which is in close agreement with the FEM-predicted average relative density of approximately 0.936. In addition, the specimen height was controlled within approximately 6.68–6.73 mm, indicating that the toroidal compacts were fabricated with comparable densification levels and dimensional consistency under the tested processing conditions. All fabricated toroidal compacts were

annealed at 720 °C for 30 min under a nitrogen atmosphere to relieve residual stress generated during compaction and to stabilize the electromagnetic response and interparticle insulation structure. Therefore, the SEM and TEM-EDS observations presented in this study reflect the microstructural characteristics of the annealed toroidal compacts after completion of the full 2P1A process. In practical bulk fabrication, maintaining consistent powder charge and compaction stability is important because specimen-to-specimen variations can directly affect electromagnetic properties and microstructural characteristics. Accordingly, the 2P1A process was applied as a staged densification route for improving fabrication stability and quality uniformity [29,30,36].

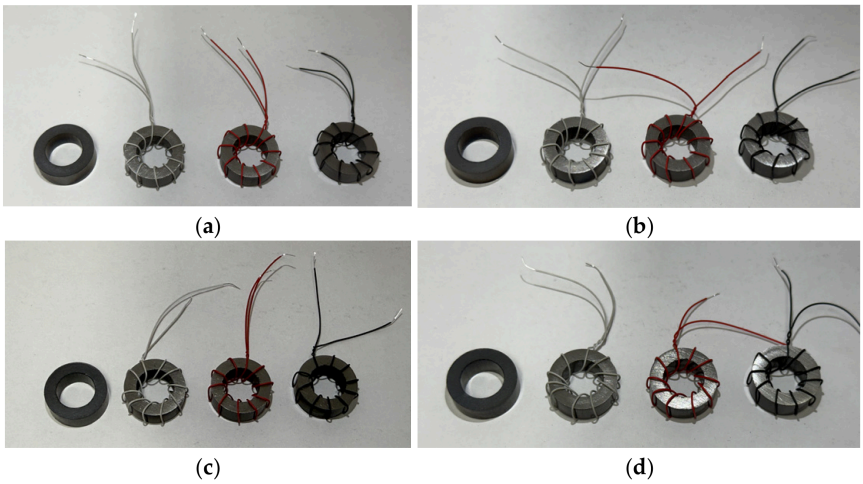


Figure 9. Fabricated Fe–5.0 wt.%Si toroidal compacts and wound specimens for electromagnetic measurements under (**a**) 550 °C single-press (Case 3), (**b**) 30% → 100% 2P1A (Case 4), (**c**) 50% → 100% 2P1A (Case 5), and (**d**) 70% → 100% 2P1A (Case 6) conditions.

4.2. Evaluation of Electromagnetic Properties

Frequency-dependent electromagnetic properties were measured to compare the magnetic response of the single-press and 2P1A toroidal compacts. A 10-turn copper coil was wound around each toroidal specimen, and the inductance L and equivalent series resistance R were measured over the frequency range of 0.5–20 kHz using a Precision LCR meter (4284A, Agilent Technologies, Santa Clara, CA, USA) [26,31].

The Q-factor was calculated as the ratio of inductive reactance to equivalent series resistance, as expressed in Equation (2).

$$Q(f) = \frac{X_L}{R} = \frac{2\pi f L}{R}, \tag{2}$$

here f, X_L, L, and R denote the measurement frequency, inductive reactance, inductance, and equivalent series resistance, respectively.

The relative permeability was calculated from the inductance relation of the toroidal magnetic core. The inductance of a toroidal core is expressed as Equation (3).

$$L = \frac{\mu_0 \mu_r N^2 A_e}{l_e}. \tag{3}$$

Therefore, the relative permeability was calculated using Equation (4).

$$\mu_r = \frac{L}{\mu_0 N^2} \cdot \frac{l_e}{A_e}, \tag{4}$$

here μ_0, N, A_e, and l_e denote the permeability of free space, number of turns, effective cross-sectional area, and effective magnetic path length, respectively. In this study, the measured inductance was converted into effective relative permeability according to the toroidal core geometry. Inductance was used as an intermediate measured parameter for permeability calculation, and the results were interpreted based on effective relative permeability and Q-factor. The results were interpreted based on effective relative permeability and Q-factor over the frequency range of 0.5–20 kHz.

4.2.1. Effective Relative Permeability

Effective relative permeability is an index that represents the degree of magnetization of a compact under an external magnetic field under identical toroidal geometry and winding conditions. In SMC cores, permeability is affected not only by final density, but also by interparticle contact state, insulation layer continuity, residual stress, pore distribution, and local densification uniformity. Therefore, the frequency-dependent retention of permeability is important for evaluating the stability of the magnetic path inside the compact.

Figure 10a shows the effective relative permeability of the single-press and 2P1A toroidal compacts. At 1 kHz, the 30% → 100% 2P1A condition exhibited the highest permeability of approximately 145, while the 50% → 100% and 70% → 100% 2P1A conditions showed values of approximately 135 and 137, respectively. The 550 °C single-press condition showed a permeability of approximately 139, indicating that the magnetic response was comparable among all conditions in the low-frequency range.

However, the difference between the conditions became more evident as the frequency increased to 20 kHz. The permeability of the 550 °C single-press condition decreased to approximately 114, whereas the 30% → 100%, 50% → 100%, and 70% → 100% 2P1A conditions maintained values of approximately 141, 134, and 137, respectively. This result indicates that the decrease in permeability with increasing frequency was suppressed under the 2P1A conditions.

4.2.2. Quality Factor

The Q-factor represents the ratio of the inductive component to the resistive loss component in the alternating magnetic response of a toroidal core. Under identical geometry and winding conditions, a higher Q-factor indicates that the magnetic energy storage component is more dominant than the loss component, making it suitable for comparing the frequency-dependent electromagnetic properties of SMC cores [26,31].

Figure 10b shows the variation in Q-factor with frequency. In the low-frequency range of 1–2 kHz, the differences between the conditions were limited. At 2 kHz, the Q-factor values of the 30% → 100%, 50% → 100%, and 70% → 100% 2P1A conditions were 1.61, 1.53, and 1.55, respectively, which were comparable to that of the 550 °C single-press condition at 1.48. However, above 5 kHz, the Q-factor values of the 2P1A conditions remained higher than that of the single-press condition. At 20 kHz, the Q-factor values of the 30% → 100%, 50% → 100%, and 70% → 100% 2P1A conditions were 5.05, 7.23, and 8.63, respectively, corresponding to increases of approximately 136%, 238%, and 303% compared with the 550 °C single-press condition at 2.14. In particular, the 70% → 100% 2P1A condition exhibited the highest Q-factor at 20 kHz, indicating that the inductive response was maintained more effectively in the higher-frequency range.

4.2.3. Permeability Retention Ratio

The permeability retention ratio was used to compare the ability to maintain effective relative permeability with increasing frequency and was calculated as the ratio of permeability at 20 kHz to that at 1 kHz.

As shown in Figure 10c, the permeability retention ratios of the 30% → 100%, 50% → 100%, and 70% → 100% 2P1A conditions were 97.2%, 99.3%, and 100.0%, respectively, which were higher than that of the 550 °C single-press condition at 82.0%. This result indicates that the 2P1A compacts maintained permeability more stably with increasing frequency.

The permeability retention and Q-factor results show that the 2P1A conditions maintained more stable electromagnetic behavior than the 550 °C single-press condition in the 5–20 kHz range. In the 2P1A process, densification proceeded through separated 1st and 2nd pressing stages, which may influence the interparticle contact state and local densification distribution. This staged compaction path can be associated with the reduced decrease in permeability and the higher Q-factor values observed with increasing frequency. In the 550 °C single-press condition, the densification process was completed in one pressing stage, which may lead to localized densification and stress concentration. These local non-uniformities can decrease magnetic path stability at higher frequencies and increase the loss component, resulting in lower permeability retention and Q-factor. The repeated measurements summarized in Supplementary Table S1 also support this trend. The differences in permeability retention ratio and Q-factor between the single-press and 2P1A conditions were larger than the specimen-to-specimen variations within each condition, indicating that the improved electromagnetic response was mainly associated with the 2P1A processing condition.

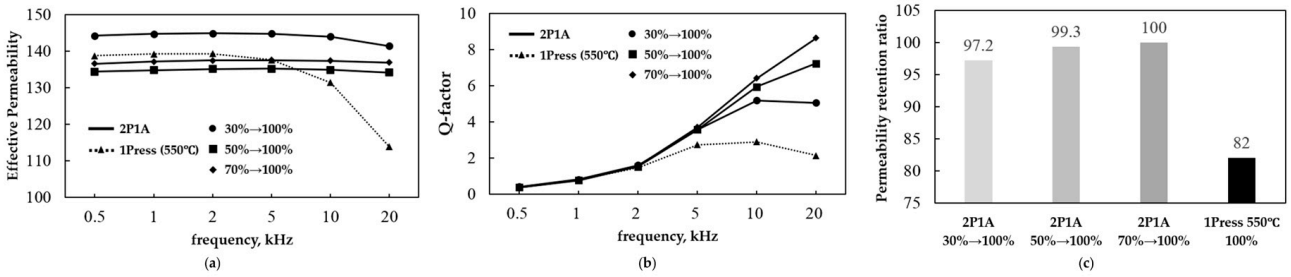


Figure 10. Frequency-dependent electromagnetic properties of single-press and 2P1A toroidal compacts: (**a**) effective relative permeability, (**b**) Q-factor, and (**c**) permeability retention ratio at 20 kHz normalized to the 1 kHz permeability.

4.3. Microstructural Characterization of 2P1A Compacts

4.3.1. Local Densification and Pore Morphology

The microstructure of the toroidal compacts was analyzed at the upper and lower regions to examine the relationship between the local densification behavior obtained from FEM analysis and the actual interparticle contact and pore morphology. The SEM observations were conducted using a scanning electron microscope (SEM; JEOL Ltd., Tokyo, Japan). In the 2P1A process, the local relative density and hydrostatic stress distributions at the upper and lower regions varied depending on the 1st pressing level. SEM analysis was used to compare the pore morphology and interparticle contact state at the upper and lower regions of each compact. Figure 11 shows the upper and lower evaluation regions defined in the FEM local relative density analysis together with the corresponding local relative density results under each condition, while Figure 12 presents the corresponding SEM microstructural observations.

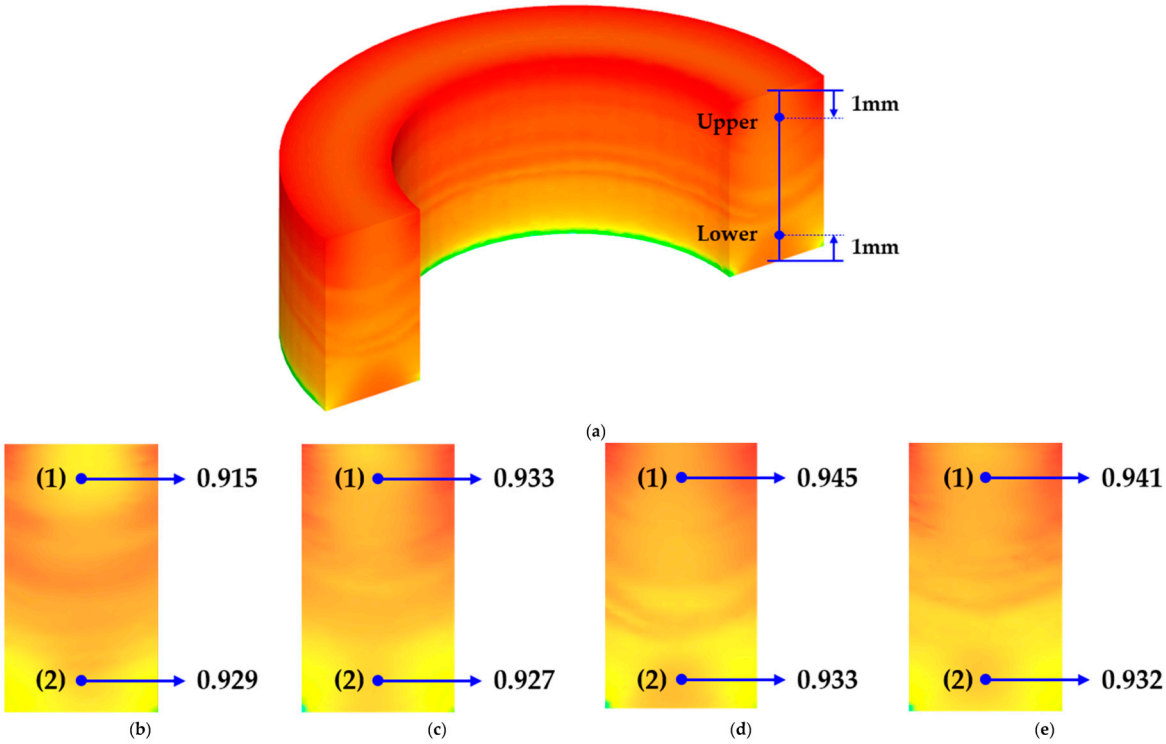


Figure 11. FEM analysis of local relative density at the upper and lower regions of Fe–5.0 wt.%Si toroidal compacts: (**a**) definition of the upper and lower evaluation points, (**b**) 30% → 100% 2P1A (Case 4), (**c**) 50% → 100% 2P1A (Case 5), (**d**) 70% → 100% 2P1A (Case 6), and (**e**) 550 °C single-press (Case 3).

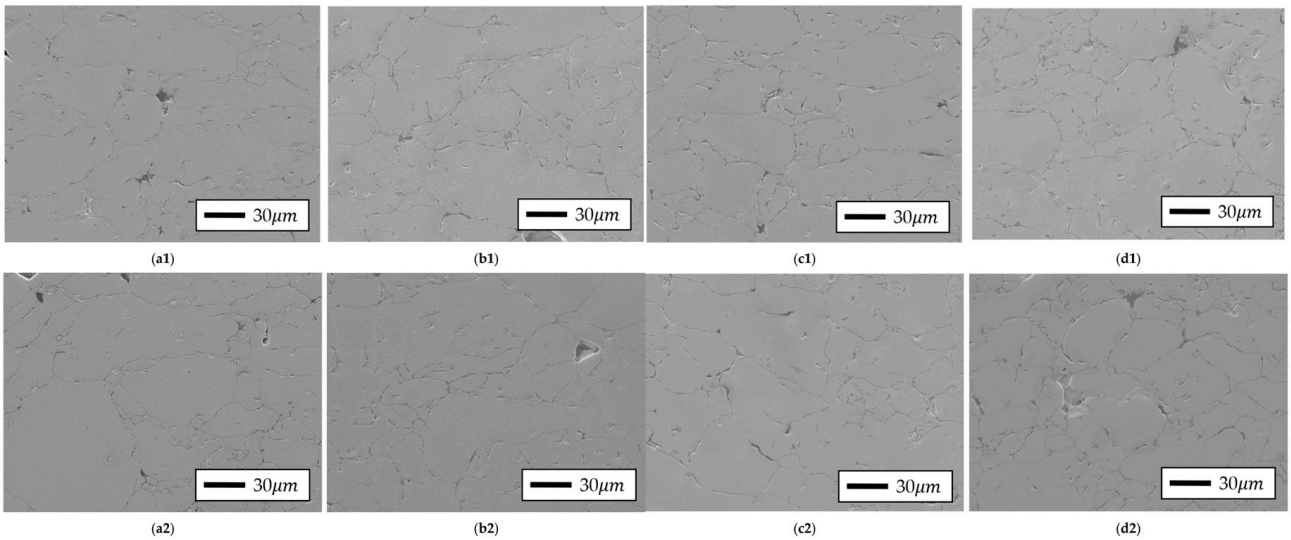


Figure 12. SEM results corresponding to the upper and lower points of Fe–5.0 wt.%Si toroidal compacts under different compaction conditions: (**a1**,**a2**) 30–100% 2P1A (Case 4), (**b1**,**b2**) 50–100% 2P1A (Case 5), (**c1**,**c2**) 70–100% 2P1A (Case 6), and (**d1**,**d2**) 550 °C single-press (Case 3).

Under the 30% → 100% 2P1A condition, the densification difference between the upper and lower regions was also observed in the SEM results. The FEM local relative densities were 0.915 and 0.929 at the upper and lower regions, respectively, corresponding to a difference of approximately 0.014. The upper region in Figure 12(a1) exhibited more pronounced interparticle gaps and localized pores than the lower region in Figure 12(a2), whereas the lower region showed a more continuous particle contact structure. These

observations indicate that the upper/lower densification difference formed under the low 1st pressing level condition was reflected in the actual pore morphology and interparticle contact state.

The smallest upper/lower density difference was observed under the 50% → 100% 2P1A condition. The FEM local relative densities were 0.933 and 0.927 at the upper and lower regions, respectively. The SEM results in Figure 12(b1,b2) also showed limited differences in pore distribution and particle packing morphology between the two regions, and the interparticle contact structure remained comparatively uniform. These results suggest that this 1st pressing level produced the most stable local structural uniformity.

Under the 70% → 100% 2P1A condition, local densification became more concentrated near the upper region. The FEM local relative densities were 0.945 and 0.933 at the upper and lower regions, respectively, together with a relatively high hydrostatic stress level. The upper region in Figure 12(c1) showed a dense particle contact morphology with reduced pore distribution, whereas the lower region in Figure 12(c2) partially exhibited elongated interparticle gaps. This result indicates that the high 1st pressing level condition intensified local densification near the upper region.

The 550 °C single-press condition exhibited local relative densities of 0.941 and 0.932 at the upper and lower regions, respectively. The SEM results in Figure 12(d1,d2) also showed a stable particle contact structure throughout the compact. In particular, the upper region exhibited a dense interparticle contact morphology corresponding to the high local relative density and compressive stress state. No severe localized pore concentration was observed in either region, and the pore distribution remained comparatively uniform.

Overall, the SEM observations showed microstructural trends qualitatively consistent with the local relative density and hydrostatic stress distributions obtained from the FEM analysis. Regions with higher local relative density and compressive stress exhibited denser interparticle contact structures with reduced pore distribution, whereas regions with relatively lower density showed more pronounced interparticle gaps and localized pores. In particular, the 50% → 100% 2P1A condition exhibited the smallest upper/lower density difference and relatively small differences in pore morphology and particle contact between the two regions, indicating the most uniform local structure among the investigated conditions. Therefore, the SEM results demonstrate that the local densification behavior predicted by FEM analysis was reflected in the actual pore distribution and interparticle contact morphology inside the bulk compact, confirming that the 1st pressing level in the 2P1A process is an important processing parameter affecting the structural uniformity of the final compact.

4.3.2. Interparticle Insulation Structure

Representative TEM images and EDS maps of the interparticle boundary regions are presented in Figures 13–16, and the measured interfacial thicknesses are summarized in Table 7. For each condition, two lamella regions were analyzed, and ten interfacial thickness measurements were obtained from each lamella. The thickness values indicated in the TEM images correspond to representative measurements close to the average thickness of each lamella [37].

The EDS maps showed that O and Si were distributed along the interparticle boundaries in all investigated conditions, while P was detected in the same boundary regions. These observations indicate that the insulation-related interfacial structure was retained after compaction and annealing. Differences among the investigated conditions were observed primarily in the boundary morphology and interfacial thickness distribution rather than in the overall elemental distributions.

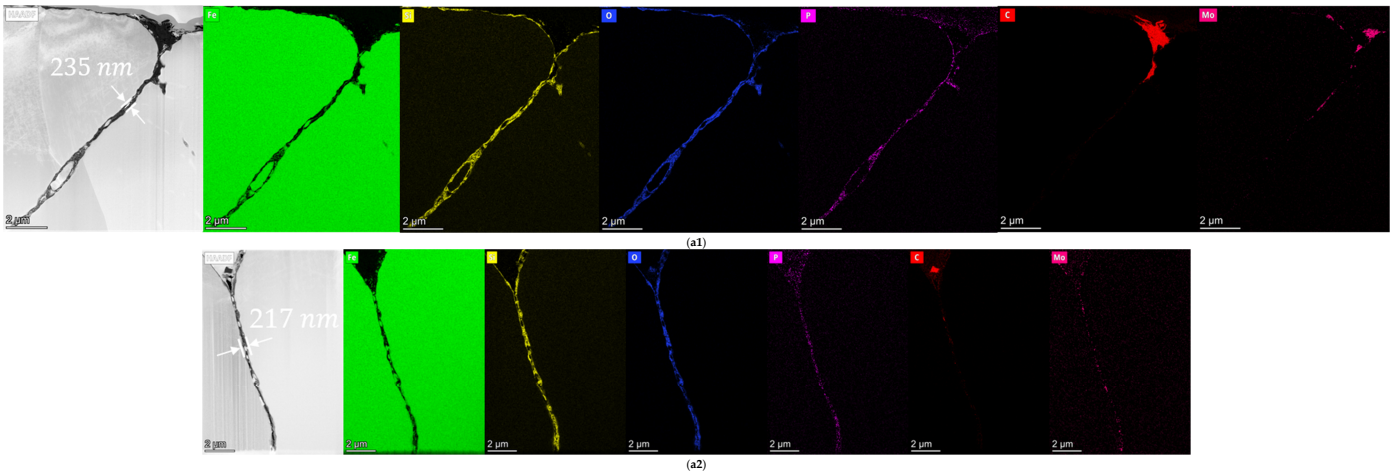


Figure 13. TEM-EDS analysis of two representative interparticle boundary regions in the 30% → 100% 2P1A condition: (**a1**,**a2**) TEM images and corresponding EDS elemental distributions of Fe, Si, O, P, C, and Mo.

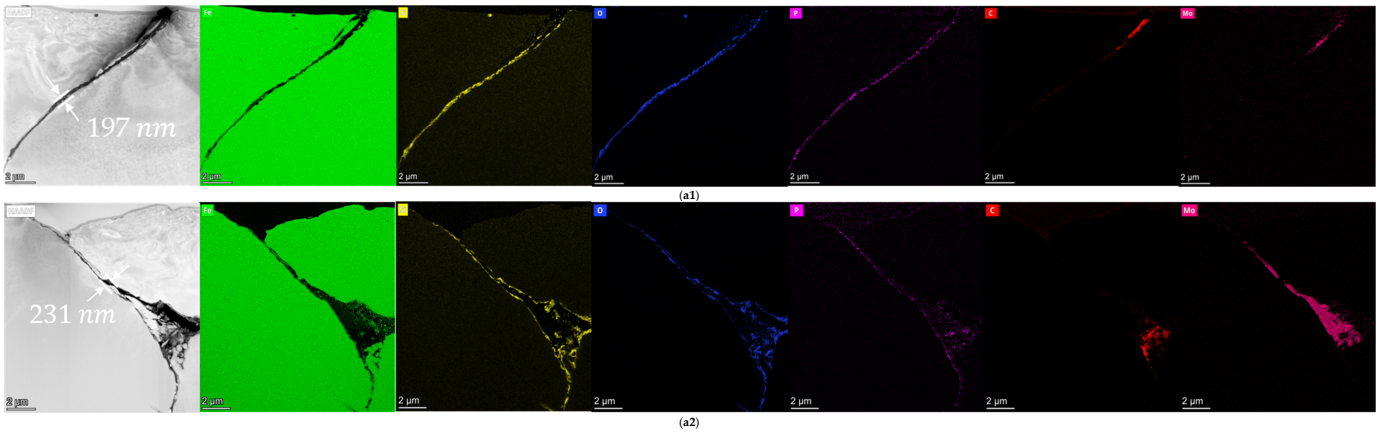


Figure 14. TEM-EDS analysis of two representative interparticle boundary regions in the 50% → 100% 2P1A condition: (**a1**,**a2**) TEM images and corresponding EDS elemental distributions of Fe, Si, O, P, C, and Mo.

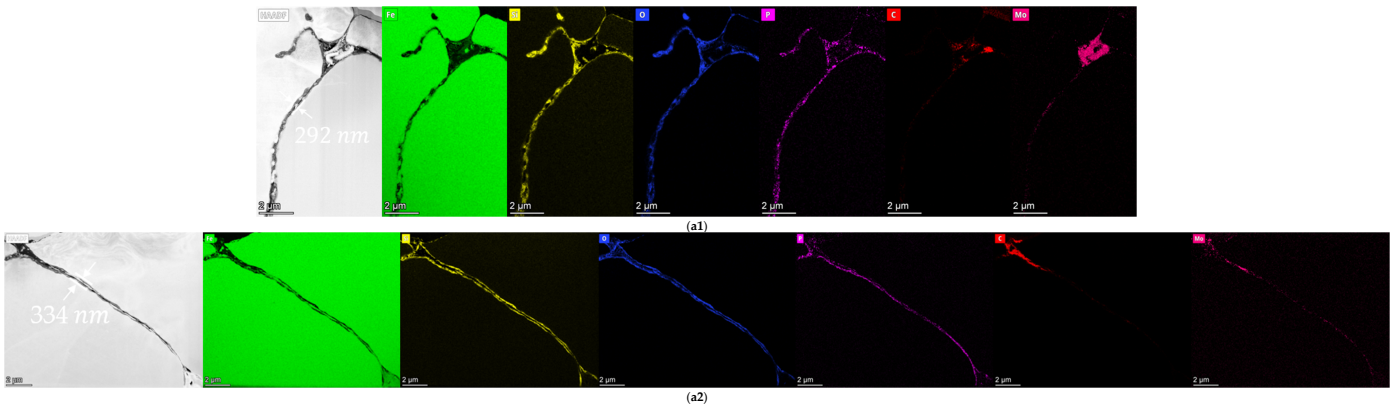


Figure 15. TEM-EDS analysis of two representative interparticle boundary regions in the 70% → 100% 2P1A condition: (**a1**,**a2**) TEM images and corresponding EDS elemental distributions of Fe, Si, O, P, C, and Mo.

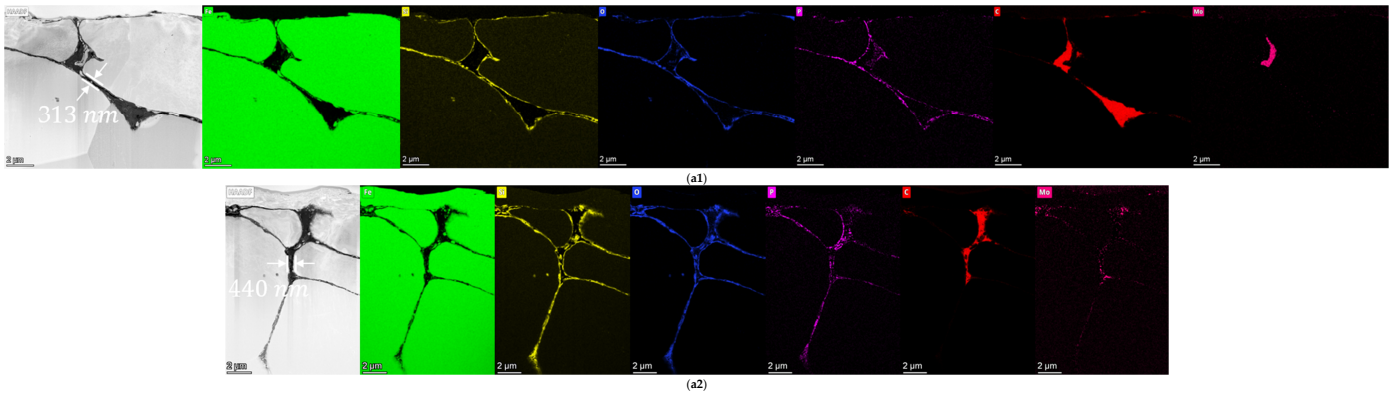


Figure 16. TEM-EDS analysis of two representative interparticle boundary regions in the 550 °C single-press condition: (**a1**,**a2**) TEM images and corresponding EDS elemental distributions of Fe, Si, O, P, C, and Mo.

Table 7. Measured insulation layer thicknesses of the investigated conditions shown in Figures 13–16.

Condition	Region	Mean (nm)	Range (nm)
30% → 100%	Figure 13(a1)	220.3	111–449
2P1A	Figure 13(a2)	226.0	147–301
50% → 100%	Figure 14(a1)	202.7	100–361
2P1A	Figure 14(a2)	235.2	110–316
70% → 100%	Figure 15(a1)	260.7	118–598
2P1A	Figure 15(a2)	321.1	157–457
550 °C	Figure 16(a1)	336.2	93–1170
Single Press	Figure 16(a2)	339.1	84–854

Among the 2P1A conditions, the 50% → 100% condition exhibited the lowest average interfacial thickness and the narrowest thickness range. The interfacial layer appeared relatively continuous within the analyzed lamella regions, and no pronounced pore-like boundary opening was observed. The 30% → 100% condition showed a similar average thickness but a wider thickness range, together with locally opened boundary regions. In the 70% → 100% condition, both the average thickness and thickness range increased, and locally thickened interfacial regions were observed near several particle junctions.

The most noticeable difference was observed in the 550 °C single-press condition. Compared with the 2P1A conditions, this condition exhibited a substantially wider thickness range, together with locally widened interfaces and pore-like boundary structures. In addition, C-rich regions were observed near several widened boundaries and junctions.

Overall, the TEM-EDS results showed that an insulation-related interparticle boundary structure containing Si, O, and P was maintained in all investigated conditions. Although the overall elemental distributions were similar, differences were observed in the local interfacial morphology and interfacial thickness distribution depending on the compaction route. In particular, the 2P1A conditions generally exhibited narrower thickness distributions than the 550 °C single-press condition, suggesting that the staged compaction route influenced the development of the interparticle boundary structure during compaction and subsequent annealing.

5. Conclusions

In this study, the effect of the 1st pressing level on the final densification state, interparticle insulation structure, and high-frequency electromagnetic response was evaluated in the 2P1A compaction of Fe–5.0 wt.%Si SMC toroidal cores. The 30% → 100% and 50% →

100% conditions showed similar relative density differences of 0.33 and 0.34, respectively, whereas the 70% → 100% condition exhibited the largest relative density difference of 0.43, along with the highest final reaction load of 6.46 tons and average hydrostatic stress of −467.07 MPa. This result indicates that a higher 1st pressing level does not necessarily ensure improved final densification uniformity but can increase compaction resistance and stress accumulation during the 2nd pressing stage. In the fabricated compacts, the local densification tendency was reflected in the interparticle contact state and pore morphology, and the interparticle boundary structure containing O and Si was retained under all conditions. In particular, the 50% → 100% condition showed the lowest average insulation layer thickness and the narrowest thickness range among the analyzed TEM regions, indicating the most balanced condition among the 2P1A conditions in terms of densification uniformity and insulation-layer thickness distribution. In terms of electromagnetic properties, the 2P1A conditions exhibited better high-frequency retention than the 550 °C single-press condition; the permeability retention ratio increased from 82.0% to 97.2–100.0%, and the Q-factor at 20 kHz increased from 2.14 to 5.05–8.63. Therefore, in the 2P1A compaction of Fe–5.0 wt.%Si SMCs, setting the 1st pressing level that determines the densification state before the 2nd pressing stage is important, and the 50% → 100% condition was identified as the most balanced condition within the investigated range when structural uniformity and high-frequency electromagnetic response were considered together. Future work will apply the 1st pressing level-controlled 2P1A condition identified in this study to actual SMC stator core geometries for motor applications and further evaluate the local density distribution, insulation-layer retention, and electromagnetic response in the practical operating frequency range.

Supplementary Materials: The following supporting information can be downloaded at: https://www.mdpi.com/article/10.3390/met16060669/s1, Table S1: Experimental data for bulk density and electromagnetic properties of the fabricated toroidal specimens.

Author Contributions: Conceptualization, S.L.; methodology, M.S. and S.L.; software, M.S.; validation, M.S. and S.L.; formal analysis, M.S. and S.L.; investigation, M.S. and S.L.; resources, S.L.; data curation, M.S.; writing—original draft preparation, M.S.; writing—review and editing, S.L.; visualization, M.S.; supervision, S.L.; project administration, S.L.; funding acquisition, S.L. All authors have read and agreed to the published version of the manuscript.

Funding: This research was supported by Korea Institute for Advancement of Technology (KIAT) grant funded by the Korea Government (MOTIE). (P0020536, HRD Program for Industrial Innovation).

Data Availability Statement: The original contributions presented in this study are included in the article/Supplementary Material. Further inquiries can be directed to the corresponding author.

Conflicts of Interest: The authors declare no conflicts of interest.

References

1. Shokrollahi, H.; Janghorban, K. Soft magnetic composite materials (SMCs). *J. Mater. Process. Technol.* **2007**, *189*, 1–12. [CrossRef]
2. Périgo, E.A.; Weidenfeller, B.; Kollár, P.; Füzer, J. Past, present, and future of soft magnetic composites. *Appl. Phys. Rev.* **2018**, *5*, 031301. [CrossRef]
3. Guo, Y.; Ba, X.; Liu, L.; Lu, H.; Lei, G.; Yin, W.; Zhu, J. A Review of Electric Motors with Soft Magnetic Composite Cores for Electric Drives. *Energies* **2023**, *16*, 2053. [CrossRef]
4. Baitalyuk, B.S.; Nosenko, V.K.; Yevlash, I.K.; Nosenko, A.V.; Iakovlev, V.E.; Dekhtyarenko, V.A. Powder Soft Magnetic Composites: Problems and Prospects. *Phys. Met. Metallogr.* **2024**, *125*, 50–83.
5. Silveyra, J.M.; Ferrara, E.; Huber, D.L.; Monson, T.C. Soft magnetic materials for a sustainable and electrified world. *Science* **2018**, *362*, eaao0195. [CrossRef] [PubMed]
6. Krings, A.; Boglietti, A.; Cavagnino, A.; Sprague, S. Soft Magnetic Material Status and Trends in Electric Machines. *IEEE Trans. Ind. Electron.* **2017**, *64*, 2405–2414. [CrossRef]

7. Wang, W.; Fan, J.; Li, C.; Yu, Y.; Wang, A.; Li, S.; Liu, J. Low-Loss Soft Magnetic Materials and Their Application in Power Conversion: Progress and Perspective. *Energies* **2025**, *18*, 482. [CrossRef]
8. Kang, S.; Lee, S. Optimizing the Manufacturing Process Control of Si-Based Soft Magnetic Composites. *Materials* **2025**, *18*, 2321. [CrossRef] [PubMed]
9. Cotojman, L.; Marinca, T.; Chicinaş, I.; Popa, F.; Neamțu, B.V.; Pricǎ, V.C. Producing Soft Magnetic Composites by Spark Plasma Sintering of Pseudo Core–Shell Ni–Fe Alloy@$Mn_{0.5}Zn_{0.5}Fe_2O_4$ Powders. *Materials* **2023**, *16*, 501. [CrossRef] [PubMed]
10. Li, S.; Peng, K.; Zou, L. The improved magnetic properties of FeSi powder cores composed of different size particles. *J. Mater. Sci. Mater. Electron.* **2022**, *33*, 607–616. [CrossRef]
11. Wang, S.; Zheng, J.; Zheng, D.; Qiao, L.; Ying, Y.; Tang, Y.; Cai, W.; Li, W.; Yu, J.; Li, J.; et al. Low Core Losses of Fe-Based Soft Magnetic Composites with an Zn–O–Si Insulating Layer Obtained by Coupling Synergistic Photodecomposition. *Materials* **2022**, *15*, 8660. [CrossRef] [PubMed]
12. Arif, M.; Han, D.; Shin, W.; Cha, S.; Pak, C.; Kim, Y.; Kim, S.; Lee, B.; Rhyee, J. Ultra-Low Core Loss and High-Frequency Permeability Stability in Hot-Press Sintered FeSi Soft Magnetic Composites by Fe2O3 Nanoparticles Air Gap Filling. *Materials* **2025**, *18*, 2013. [CrossRef]
13. Sun, X.-K.; Chen, S.-J.; Xu, J.-Z.; Zhen, L.-D.; Kim, K.-T. Analysis of cold compaction densification behaviour of metal powders. *Mater. Sci. Eng. A* **1999**, *267*, 43–49. [CrossRef]
14. Kang, C.S.; Kim, K.T.; Lee, S.C.; Rozenberg, O. Densification Behavior of Iron Powder during Cold Stepped Compaction. *Mater. Sci. Forum* **2007**, *534–536*, 257–260. [CrossRef]
15. Sofuoğlu, H.; Güçlü, R. Numerical Modeling of Cold Powder Compaction Using Multi-Particle and Continuum Media Approaches. *Powder Technol.* **2015**, *271*, 238–247. [CrossRef]
16. Hsiang, H.-I. Phosphoric acid addition effect on the microstructure and magnetic properties of iron-based soft magnetic composites. *J. Magn. Magn. Mater.* **2018**, *447*, 1–8. [CrossRef]
17. Shima, S.; Oyane, M. Plasticity Theory for Porous Metals. *Int. J. Mech. Sci.* **1976**, *18*, 285–291. [CrossRef]
18. Zhang, S.; Chen, X. Deduction of a porosity-dependent yield criterion and its geometrical description for porous materials. *Int. J. Mech. Sci.* **2014**, *89*, 58–68. [CrossRef]
19. Zhang, W.; Zhang, S.; Tan, J.; Du, J.; Zhang, N. Investigation on the friction mechanism and its relation to the force chains during powder compaction. *J. Phys. Soc. Jpn.* **2020**, *89*, 124602. [CrossRef]
20. Camurlu, H.E.; Karomatullozoda, L. Warm Compaction of Iron Powder. *Mater. Sci. Non-Equilib. Phase Transform.* **2019**, *5*, 120–122.
21. Yang, Y.; Wang, Y.; Wu, S.; Liu, C.; Chen, L. Core Loss Analysis of Soft Magnetic Composites Considering the Inter-Particle Eddy Current Loss. *AIP Adv.* **2021**, *11*, 015140. [CrossRef]
22. *IEC 60404-6:2018*; Magnetic Materials—Part 6: Methods of Measurement of the Magnetic Properties of Magnetically Soft Metallic and Powder Materials at Frequencies in the Range 20 Hz to 100 kHz by the Use of Ring Specimens. International Electrotechnical Commission: Geneva, Switzerland, 2018.
23. Ahmed, N.; Atkinson, G.J. A Review of Soft Magnetic Composite Materials and Applications. In Proceedings of the 2022 International Conference on Electrical Machines (ICEM), Valencia, Spain, 5–8 September 2022; pp. 551–557. [CrossRef]
24. Sim, M.; Lee, S. A Study on the Influence of the Properties of Commercial Soft Magnetic Composite Somaloy Materials on the Compaction Process. *Appl. Mech.* **2025**, *6*, 65. [CrossRef]
25. Kang, S.; Lee, S. Formability and Electromagnetic Performance Comparison of Fe–P-Based SMC and Fe–5.0 wt.%Si Powders. *Materials* **2025**, *18*, 4405. [CrossRef]
26. Wang, X.; Ge, H. Improved permeability and core loss of iron-based soft magnetic composites prepared by interface diffusion of nitrogen atoms. *Mater. Today Commun.* **2024**, *38*, 108161.
27. Li, H.; Yang, L.; Li, Z.; Li, Z.; Liu, X. Multifunctional FeSiAl Soft Magnetic Composites with Inorganic–Organic Hybrid Insulating Layers for High-Frequency Inductors. *J. Electron. Mater.* **2022**, *51*, 5967–5979. [CrossRef]
28. Bureš, R.; Milyutin, V.A.; Faberova, M.; Bircakova, Z.; Kollar, P.; Fuzer, J. The First Experimentally Obtained Dataset on Processing Parameters and Properties of Soft Magnetic Composites. *Sci. Data* **2024**, *11*, 8.
29. Nie, M.; Jiang, C.; Yang, Y.; Zhou, B.; Chen, Z.; Jia, G.; Li, Z.; Dai, C.; He, J.; Guo, H. Multicomponent Soft Magnetic Alloys for Soft Magnetic Composites: A Review. *Mater. Today Electron.* **2025**, *12*, 100153. [CrossRef]
30. Rodriguez-Sotelo, D.; Rodriguez-Licea, M.A.; Araujo-Vargas, I.; Prado-Olivarez, J.; Barranco-Gutiérrez, A.-I.; Perez-Pinal, F.J. Power Losses Models for Magnetic Cores: A Review. *Micromachines* **2022**, *13*, 418. [CrossRef] [PubMed]
31. Xu, Z.; Wang, C. Measurement of Permeability and Q-Factor of Ferrite Toroids. *High Power Laser Part. Beams* **2005**, *17*, 181–184.
32. Rahman, M.M.; Nor, S.S.M.; Ariffin, A.K. Effect of Lubricant Content to the Properties of Fe-Based Powder Compacts at Warm Compaction. *Mater. Sci. Eng. A* **2010**, *527*, 7183–7189.
33. Hu, X.; Liu, Z.; Liu, X.; Xie, H.; Zhang, C.; Zou, Y. Effect of Warm Compaction and Lubricant on Microstructure and Properties of Iron-Based Alloy. *J. Mater. Eng. Perform.* **2022**, *31*, 1685–1697. [CrossRef]

34. Kumar, R.; Hussainova, I.; Rahmani, R.; Antonov, M. Solid lubrication at high temperatures—A review. *Materials* **2022**, *15*, 1695. [CrossRef] [PubMed]
35. Huang, H.; Zhang, R.; Sun, H.; Wang, J. High density Fe-based soft magnetic composites with nice magnetic properties prepared by warm compaction. *J. Alloys Compd.* **2023**, *947*, 169460. [CrossRef]
36. Zhang, R.; Huang, H.; Sun, H.; Wang, J. Enhancements of magnetic properties and compacted density for Fe-based amorphous soft magnetic composites via hot compacting under an ultra-low pressure. *J. Magn. Magn. Mater.* **2024**, *601*, 171984. [CrossRef]
37. Evangelista, L.L.; Machado, L.E.; Ramos Filho, A.I.; Silva, B.S.; Hammes, G.; Binder, C.; Drago, V.; Klein, A.N. Novel soft magnetic composite with insulating layers formed in situ from hydrothermal carbon nanospheres and boric acid. *J. Alloys Compd.* **2023**, *943*, 169172. [CrossRef]

Disclaimer/Publisher's Note: The statements, opinions and data contained in all publications are solely those of the individual author(s) and contributor(s) and not of MDPI and/or the editor(s). MDPI and/or the editor(s) disclaim responsibility for any injury to people or property resulting from any ideas, methods, instructions or products referred to in the content.